ACS Catalysis

Research Article

pubs.acs.org/acscatalysis

Ultrathin $MoS_{2(1-x)}Se_{2x}$ Alloy Nanoflakes For Electrocatalytic Hydrogen Evolution Reaction

Qiufang Gong,[†,§] Liang Cheng,[†,§] Changhai Liu,[†] Mei Zhang,[‡] Qingliang Feng,[‡] Hualin Ye,[†] Min Zeng,[†] Liming Xie,[‡] Zhuang Liu,*[,†] and Yanguang Li*[,†]

[†]Institute of Functional Nano & Soft Materials (FUNSOM), Soochow University, Suzhou 215123, People's Republic of China

[‡]CAS Key Laboratory of Standardization and Measurement for Nanotechnology, National Center for Nanoscience and Technology, Beijing 100190, People's Republic of China

Supporting Information

ABSTRACT: The development of non precious metal based electrocatalysts for the hydrogen evolution reaction (HER) holds a decisive key to a spectrum of energy conversion technologies. Previous studies have established layered molybdenum chalcogenides as promising candidates. In this work, we prepared ultrathin $MoS_{2(1-x)}Se_{2x}$ alloy nanoflakes with monolayer or few-layer thickness and fully tunable chemical composition for maximum HER activity. Spectroscopic characterizations corroborate the progressive evolution of their structures and properties as x increases from 0 to 1 without any noticeable phase separation. In particular, it is evidenced that the introduction of selenium continuously modulates the d band electronic structure of molybdenum, probably leading to tuned hydrogen adsorption free energy and consequently electrocatalytic activity. Electrochemical measurements show that all $MoS_{2(1-x)}Se_{2x}$ nanoflakes are highly active and durable for HER with small overpotentials in the range of 80−100 mV and negligible activity loss up to 10000 cycles. Most importantly, alloyed nanoflakes, especially with the chemical composition of MoSSe, exhibit improved performance in comparison to either MoS_2 or $MoSe_2$. Given their overall similar nanoflake morphologies, we believe such improvements reflect the higher intrinsic activity of alloyed catalysts with the hydrogen adsorption free energy closer to thermoneutral.

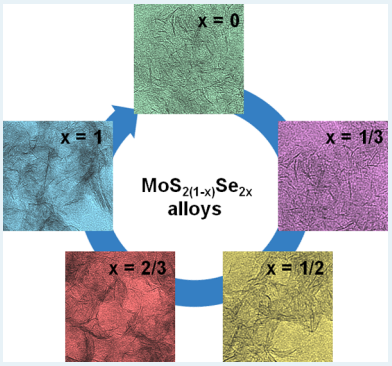

KEYWORDS: *hydrogen evolution reaction, electrocatalysis, molybdenum chalcogenides, alloys, ultrathin nanoflakes*

INTRODUCTION

The hydrogen evolution reaction (HER) is an electrochemical process in which water is reduced to molecular hydrogen.[1,2] With the increasing emphasis recently on sustainable energy harvesting and conversion, this particular reaction has gained mounting attention for its pivotal role in electrolytic or photo water splitting.[1−4] Conventionally, platinum group metals (e.g., Pt and Pd) are well documented for their high activity in catalyzing HER;[3,5] nevertheless, their wide application is essentially throttled by high costs, which would not benefit from economies of scale. Active searches have been ongoing for low-cost alternatives based on earth-abundant elements.[2−4]

Of many different candidates, layered transition metal dichalcogenides (TMDs) are especially attractive.[2,6,7] The best known example is MoS_2.[8−11] It has a structure analogous to that of graphite, wherein molybdenum atoms are sandwiched between sulfur atoms in a hexagonal arrangement; neighboring layers are bound together by weak van der Waals interactions. Theory predicts that the edge of the MoS_2 crystal has favorable hydrogen adsorption free energy (ΔG_H) and consequently high activity for HER, whereas the basal plane is electrocatalytically inert and insulating.[8] These results have been corroborated by many experimental studies.[9] In light of this structure−property relationship, structural engineering of MoS_2 crystals has been vigorously pursued with the aim to expose a greater fraction of active edges.[10−15] For example, mesoporous MoS_2 thin films with a high degree of surface curvature were reported to engender more exposed edge sites and consequently improved performance.[13] In another work, sulfurization or selenization of Mo thin films was found to yield chalcogenide films terminated with vertically aligned edges.[14] We also demonstrated that, when it was grown on graphene nanosheets, MoS_2 exhibited nanoscopic few-layer structures with abundant edges.[15] The resulting hybrid material was by far one of the best MoS_2-based HER electrocatalysts with small overpotential and Tafel slope.

In addition to structural engineering, the HER activity of TMDs can be tuned through tailoring their chemical composition. For example, cationic doping with a small fraction of cobalt or nickel is known to promote the electrocatalytic performance of MoS_2.[16] Furthermore, sulfur in MoS_2 can be partially or fully substituted with other chalcogens, leading to a library of compounds that are promising for HER. The selenium analogue $MoSe_2$ has also been found to be HER active on its edges, even though it has not received as much

Received: December 8, 2014
Revised: February 8, 2015
Published: March 2, 2015

DOI: 10.1021/cs501970w
ACS Catal. 2015, 5, 2213−2219

Table 1. Chemical Composition and Electrocatalytic Performance of Five Different $MoS_{2(1-x)}Se_{2x}$ Nanoflake Catalysts

	MoS_2	$MoS_{4/3}Se_{2/3}$	MoSSe	$MoS_{2/3}Se_{4/3}$	$MoSe_2$
Se:S ratio from ICP	0:2.00	0.65:1.35	1.03:0.97	1.34:0.66	2.00:0
η @ j = 10 mA/cm^2 (mV)	219 ± 2	172 ± 1	164 ± 2	171 ± 2	181 ± 1
Tafel slope (mV/decade)	91 ± 3	66 ± 1	48 ± 2	55 ± 1	45 ± 1
TOF @ η = 150 mV (s^{-1})	0.0401 ± 0.0050	0.0526 ± 0.0036	0.0808 ± 0.0030	0.0730 ± 0.0030	0.0556 ± 0.0065

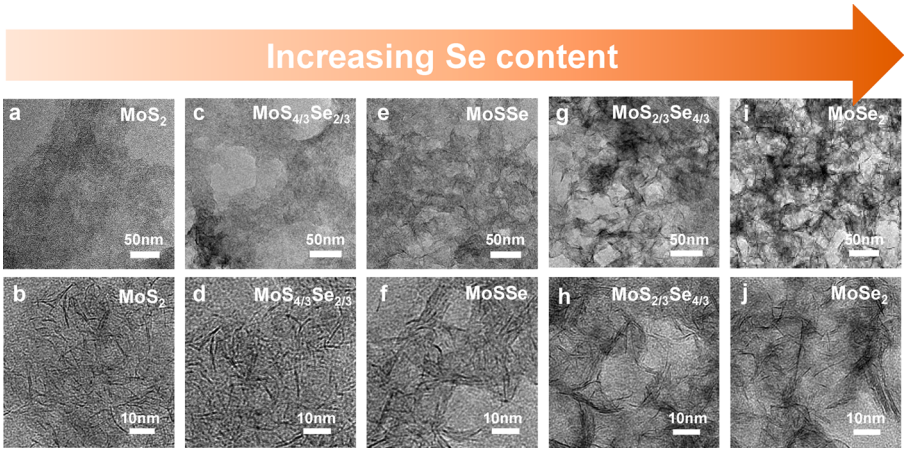

Figure 1. TEM images of $MoS_{2(1-x)}Se_{2x}$ nanoflakes with (a, b) x = 0, (c, d) x = 1/3, (e, f) x = 1/2, (g, h) x = 2/3, and (i, j) x = 1. They all possess monolayer or few-layer thicknesses and abundant edges.

attention as MoS_2 in the literature.[17−21] It has been suggested from theoretical calculations that hydrogen adsorption is slightly too weak on sulfided Mo edges (ΔG_H = 80 meV) but slightly too strong on selenided Mo edges (ΔG_H = −140 meV).[8,22] We surmise that it then may be possible to achieve a ΔG_H value close to thermoneutral ($\Delta G_H \approx 0$) by designing and exploring $MoS_{2(1-x)}Se_{2x}$ semiconductor alloys with varying Se/S ratios. Using CVD or evaporation methods at elevated temperatures (>800 °C), it is feasible to grow such alloys on substrates under careful control.[23−26] However, the preparation of $MoS_{2(1-x)}Se_{2x}$ nanostructures at low temperature and in high yields that are amenable to electrocatalytic application is currently lacking.

Very recently, our group developed a solution method to prepare monolayered WS_2 nanoflakes for HER electrocatalysis.[27] The method employs oleylamine as the solvent, which fulfills multiple functions.[27,28] It has a high solubility toward elemental sulfur, enabling the use of sulfur powder as the direct precursor; it also acts as the surfactant to passivate nanoflake surfaces and suppress their stacking. Here we demonstrate that the same method is also applicable to the synthesis of selenides and selenosulfides, in particular $MoS_{2(1-x)}Se_{2x}$ alloys with fully tunable chemical compositions and similar monolayered or few-layered nanoflake morphologies. This general synthetic method allows us to test our above hypothesis by systematically measuring and comparing the electrocatalytic activity of $MoS_{2(1-x)}Se_{2x}$ alloys for HER. We arrive at the conclusion that MoSSe is more active than either MoS_2 or $MoSe_2$.

EXPERIMENTAL SECTION

To synthesize $MoS_{2(1-x)}Se_{2x}$ nanoflakes, 1 mmol of $MoCl_5$ was first dissolved in 10 mL of oleylamine (OLA) and 10 mL of 1-octadecene (ODE), and the mixture was magnetically stirred for 20 min in a three-necked flask under an Ar atmosphere at room temperature. The solution was then heated to 140 °C and maintained at this temperature for 30 min to remove water. Subsequently, the temperature was quickly raised to 300 °C. A total 2 mmol of sulfur and/or selenium powder predissolved in 5 mL of OM was injected within 10 min. Following the injection, the solution immediately turned black. The suspension was further reacted for 1 h at 300 °C. After the mixture was naturally cooled to room temperature, products were precipitated by adding excess absolute ethanol to the reaction solution, collected by centrifugation, sequentially washed with ethanol and cyclohexane (v/v, 3/1), pure ethanol, and water, and finally lyophilized. Finally, $MoS_{2(1-x)}Se_{2x}$ nanoflakes were annealed under Ar at 400 °C for 2 h to remove organic residues adsorbed on as-made products.

Characterizations. The Se/S ratio in $MoS_{2(1-x)}Se_{2x}$ nanoflakes was analyzed by inductively coupled plasma-optical emission spectroscopy (ICP-OES). Transmission electron microscopy (TEM) and scanning transmission electron microscopy (STEM) were carried out on an FEI Tecnai F20 transmission electron microscope at an acceleration voltage of 200 kV. X-ray diffraction (XRD) patterns were obtained on a PANalytical X-ray diffractometer at a scanning rate of 0.05° s^{-1}. X-ray photoelectron spectra (XPS) was collected on an SSI S-Probe XPS spectrometer. Raman spectra of dried powder samples were taken on a Renishaw in Via plus Raman microscope with 514 nm wavelength laser excitation under 1 mV power.

Electrochemical Measurements. A 1 mg sample of $MoS_{2(1-x)}Se_{2x}$ catalyst and 0.5 mg of Ketjenblack conducting carbon black were dissolved in a mixture of 125 μL of water, 125 μL of ethanol, and 5 μL of Nafion solution (5 wt %), and the mixture was vigorously sonicated for at least 30 min to form a homogeneous catalyst ink. Then 5 μL of the catalyst ink (containing 20 μg of catalyst) was loaded onto a glassy-carbon electrode 3 mm in diameter (catalyst loading ∼0.28 mg/cm^2). Cyclic voltammetry (CV) was carried out in a standard three-electrode configuration at a scan rate of 10 mV/s with the glassy-carbon electrode, a saturated calomel electrode (SCE), and a graphite rod as the working, reference, and counter electrodes, respectively. Before each measurement, the SCE reference electrode was carefully calibrated against a reversible hydrogen electrode (RHE) from ASL in the electrolyte. Tafel plots were collected at a scan rate of 5 mV/s. Impedance measurements were performed at selected overpotentials in a frequency range of 100000−0.05 Hz. For cycling stability assessments, electrocatalysts were cycled between −0.2 and −0.4 V vs SCE at 100 mV/s.

DOI: 10.1021/cs501970w
ACS Catal. 2015, 5, 2213−2219

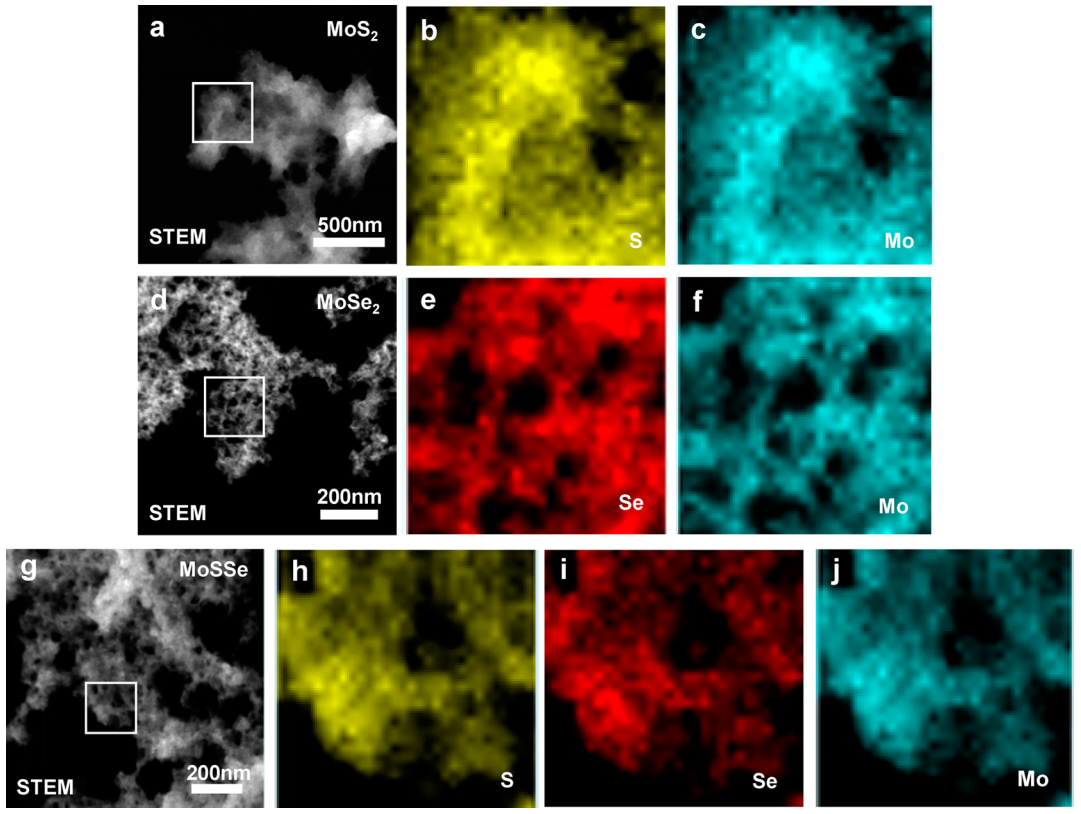

Figure 2. Spectroscopic mapping of molybdenum, sulfur, and/or selenium species within (a–c) MoS_2, (d–f) $MoSe_2$, and (g–j) MoSSe nanoflakes. The distributions of all the constituent elements show high spatial correlation.

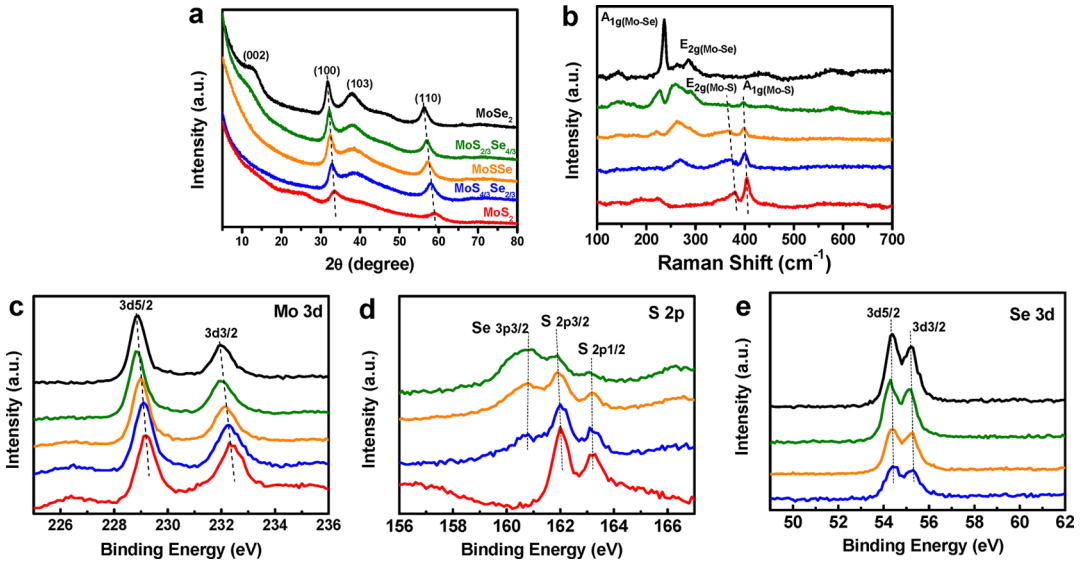

Figure 3. Spectroscopic characterizations of $MoS_{2(1-x)}Se_{2x}$ nanoflakes: (a) XRD; (b) Raman; (c–e) high-resolution XPS spectra of Mo 3d, S 2p, and Se 3d, respectively. Taken together, they corroborate the successful preparation of $MoS_{2(1-x)}Se_{2x}$ alloys with fully tunable chemical composition free of phase separation.

3. RESULTS AND DISCUSSION

We prepared $MoS_{2(1-x)}Se_{2x}$ (with x = 0, 1/3, 1/2, 2/3, and 1) nanoflakes using an established high-temperature solution method by reacting $MoCl_5$ with sulfur and/or selenium dissolved in a mixed solvent of oleylamine (OLA) and 1-octadecene (ODE) at 300 °C under N_2. OLA was selected as the main solvent for its considerable solubility toward both elemental sulfur and selenium powders and for its high boiling point desired for the synthesis.[27] It is suggested that the OLA-S or OLA-Se solution exists in the form of oleylammonium polysulfide or polyselenide, which upon heating liberates H_2S or H_2Se and reacts with the molybdenum precursor.[29,30] In addition, OLA molecules can effectively passivate the surface of resulting products, suppressing their overgrowth and aggregation, as noted previously in the synthesis of a number of sulfide or selenide nanostructures.[28] On the other hand, ODE is a

DOI: 10.1021/cs501970w
ACS Catal. 2015, 5, 2213–2219

noncoordinating solvent with low viscosity. Using the mixed solvent ODE/OLA allowed us to adjust the coordinating capability and viscosity of the solvent and consequently influence the nucleation and growth of chalcogenide nanocrystals for control over their sizes and shapes.[31] Using this strategy, we prepared MoS_2 and $MoSe_2$ nanoflakes with high yields, as well as molybdenum selenosulfides with fully tunable chemical compositions, through carefully adjusting the starting Se to S molar ratio. Inductively coupled plasma−atomic emission spectrometry (ICP-AES) analysis of the final products revealed Se:S ratios in good agreement with the starting precursors (Table 1).

Microstructures of $MoS_{2(1-x)}Se_{2x}$ alloys were examined under transmission electron microscopy (TEM) as shown in Figure 1. All of them exhibit nanoflake morphology with the dark-contrast lines representing their standing edges. Judging from the edges, these nanoflakes have monolayer or few-layer thicknesses. With increasing selenium content, the lateral dimension of individual nanoflakes grows from 10−15 nm (for x = 0 and 1/3) to mostly >20 nm (for x = 2/3 and 1); meanwhile, nanoflake thickness evolves from mostly monolayers to predominantly few-layers, probably due to the stronger interlayer interaction when the selenium fraction is higher. Previously, MoS_2 and $MoSe_2$ of different morphologies (e.g., particles, tubes, thin films and so on) have been reported.[8,16,32−34] Many of them typically form close-shell fullerene structures,[35,36] as thermodynamics dictates that the formation of electrocatalytically active edges is unfavorable compared to the formation of inert basal planes.[13] In contrast, our $MoS_{2(1-x)}Se_{2x}$ nanoflakes with monolayer or few-layer thickness possess larger surface area and abundantly exposed edges, probably stabilized via the passivation of OLA molecules during the reaction.[27] These structural features are highly advantageous to HER electrocatalysis.

To probe the spatial distribution of constituent elements within $MoS_{2(1-x)}Se_{2x}$ alloys, we carried out elemental mapping under scanning transmission electron microscopy (STEM). Representative images are summarized in Figure 2. For all five products, distributions of molybdenum and chalcogen show high spatial correlation over the entire area examined, indicative of uniform chemical compositions throughout the material. For selenosulfides, this suggests the formation of a single-phase compound with nanoscopic mixing of sulfur and selenium. No phase separation to MoS_2 and $MoSe_2$ is evidenced.

Figure 3a shows the X-ray diffraction patterns of $MoS_{2(1-x)}Se_{2x}$ alloys. All of them can be assigned to hexagonal 2H-molybdenum dichalcogenide with no discernible impurities. For the two end compositions (MoS_2 and $MoSe_2$), positions of their diffraction peaks are well consistent with standard values. Increasing the selenium content in alloys leads to a continuous downshift of all main diffraction peaks. In Figure 3a, dotted lines are added to assist in tracking the shifting of (100) and (110) peaks. This is in accordance with the gradual expansion of unit cells upon the substitution of sulfur atoms with larger selenium atoms and again implies their mixing at the atomic level. Following the shifting, the (103) peak intensity becomes more heightened. Moreover, it is also interesting to note that the (002) peaks of $MoS_{2(1-x)}Se_{2x}$ with $0 < x < 2/3$ are diminished, whereas for $MoSe_2$ (x = 1), its (002) peak is broad but still discernible. These features can be rationalized by the structural evolution from monolayer to few-layer nanoflakes when more selenium is introduced, as observed from TEM. Increased crystallographic periodicity along the c axis improves the intensity of diffraction peaks having nonzero Miller indexes along that particular direction. Moreover, all of the diffraction peaks are broadened significantly, reflecting the nanoscale dimensions of $MoS_{2(1-x)}Se_{2x}$ nanoflakes.

Further insights into the crystalline structure of $MoS_{2(1-x)}Se_{2x}$ nanoflakes were gained from Raman spectra under 514 nm laser excitation, as shown in Figure 3b. They exhibit two sets of composition-dependent vibration modes: Mo−Se related modes at low frequency (200−300 cm^{-1}) and Mo−S related modes at high frequency (350−410 cm^{-1}). Such two-mode behavior is not diagnostic of phase separation but instead is typical of $MoS_{2(1-x)}Se_{2x}$ alloys, as documented in the literature.[24−26] The Raman spectrum of MoS_2 shows strong signals from the in-plane E_{2g} (381 cm^{-1}) and the out-of-plane A_{1g} (403 cm^{-1}) vibrations. The reduced frequency difference between these two modes is characteristic of monolayer or bilayer MoS_2.[37] In addition, the large E_{2g}/A_{1g} intensity ratio indicates abundant edge structures.[20] With the introduction of selenium, the two vibration modes shift to lower frequency. It is suggested that the interaction between sulfur and selenium atoms would soften the Mo−S related modes and decrease their vibration frequency.[25,26] At the same time, Mo−Se related modes start to emerge and gain increasing intensity. Full substitution of sulfur with selenium in $MoSe_2$ results in the complete vanishing of Mo−S related modes. Its Raman spectrum features signals at 236 and 285 cm^{-1}, assignable to A_{1g} and E_{2g} vibration modes of $MoSe_2$, respectively.[24,25,38]

We also investigated the chemical states of molybdenum and chalcogen using X-ray photoelectron spectroscopy (XPS). Figure 3c−e illustrates the Mo 3d, S 2p, and Se 3d high-resolution spectra of $MoS_{2(1-x)}Se_{2x}$ nanoflakes. The Mo $3d_{5/2}$ peak located at ∼229 eV is characteristic of the Mo +4 oxidation state in the hexagonal 2H phase.[13] Introduction of selenium causes a gradual displacement of this peak to lower binding energy from 229.2 eV for MoS_2 to 228.9 eV for $MoSe_2$, consistent with a decrease in the nominal oxidation state of molybdenum when it binds to less electronegative selenium atoms.[23] This suggests that the d band electronic structure of molybdenum can be effectively modified by varying the Se:S ratio. For catalysis and electrocatalysis, d electrons in transition metals are involved in bonding with adsorbates.[39] Subtle modification in the d band electronic structure may result in an amplified change in the electrocatalytic activity of $MoS_{2(1-x)}Se_{2x}$ nanoflakes, as we shall see from a later discussion. Moreover, changes are also observed in the S 2p and Se 3d XPS spectra: with increasing selenium content, the intensity of sulfur peaks gradually diminishes whereas selenium signals rise continuously.

Taken together, the above results corroborate the successful preparation of ultrathin $MoS_{2(1-x)}Se_{2x}$ nanoflakes. Their chemical composition can readily tuned over the entire range without causing any noticeable phase separation, thus enabling one to continuously tailor their physical and chemical properties between the two end compositions. Previously, the preparation of $MoS_{2(1-x)}Se_{2x}$ alloys has been demonstrated through sulfurization and/or selenization of MoO_3 or through thermal evaporation of $MoS_2/MoSe_2$ powders at elevated temperatures >800 °C, yielding monolayer or multilayer nanosheets supported on solid substrates.[23−26] Our solution-phase synthesis is carried out at a much milder temperature with equally good composition control and higher yields. The resulting nanoflakes are rich in exposed edges, which are critical to HER electrocatalysis. Importantly, despite some slight

DOI: 10.1021/cs501970w
ACS Catal. 2015, 5, 2213−2219

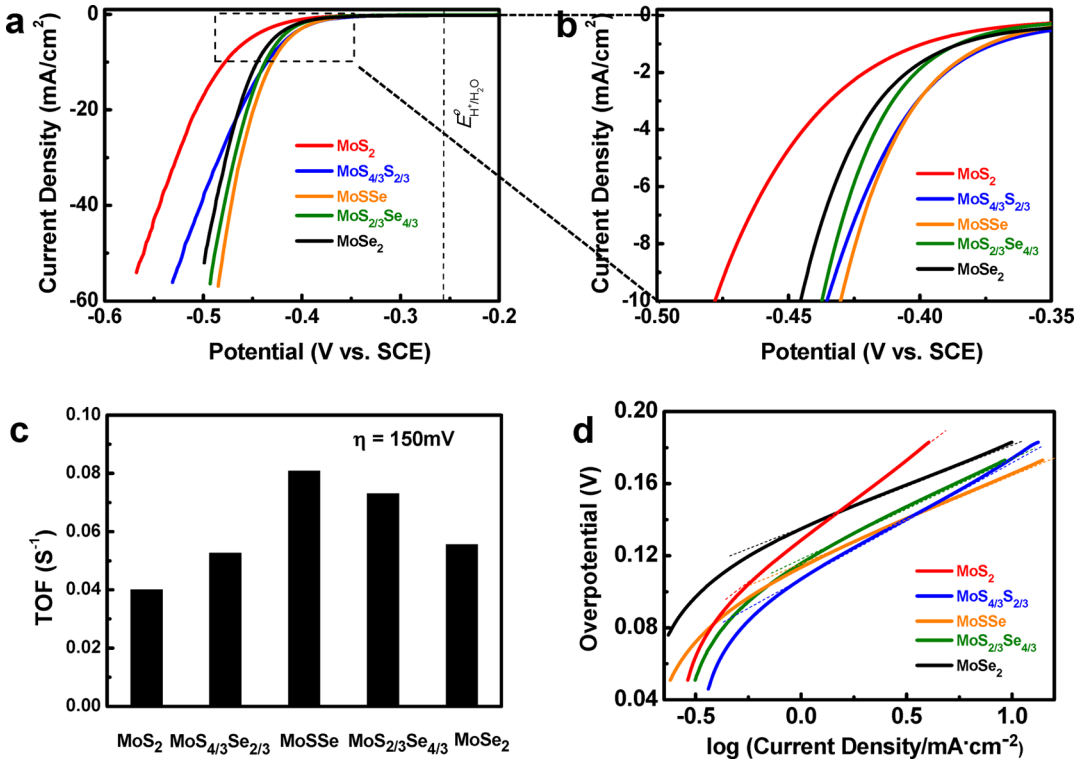

Figure 4. Electrochemical measurements of $MoS_{2(1-x)}Se_{2x}$ nanoflakes for HER electrocatalysis in 0.5 M H_2SO_4: (a, b) polarization curves, where the enclosed area of (a) is magnified in (b); (c) turnover frequency at η = 150 mV estimated from CV curves; (d) corresponding Tafel plots. Alloyed nanoflakes, particularly MoSSe, exhibit improved performance in comparison to either MoS_2 or $MoSe_2$. The vertical dotted line in (a) indicates the theoretical potential for HER.

differences (e.g., layer numbers and dimensions of nanoflakes), the morphologies of our alloyed products are similar overall. This allows us to systematically explore and compare their intrinsic electrocatalytic activities, while the influence from material microstructures is much diluted.

The electrocatalytic HER activity of $MoS_{2(1-x)}Se_{2x}$ nanoflakes was assessed in 0.5 M H_2SO_4 solution using a standard three-electrode setup. Active materials were blended with carbon black additive and Nafion polymer binder and then dropcast onto glassy-carbon electrodes. All of the data were repeated over 10 times from samples synthesized from at least three individual batches. Figure 4a,b shows the polarization curves of final products with five different compositions normalized to the geometric area of the electrode. They exhibit robust HER activity with onset potentials in the range of −0.38 to −0.35 V vs SCE, corresponding to small overpotentials of 80−110 mV. Cathodic current densities rise rapidly beyond these onsets, accompanied by visible H_2 bubbles evolving from the electrode surface. Importantly, we found the Ar annealing step was critical to ensure the high HER activity of nanoflake catalysts (Figure S1 in the Supporting Information).

We then quantified the electrocatalytic activity by overpotentials required to reduce water at a current density of 10 mA/cm^2—a metric relevant to solar fuel synthesis (Table 1). MoS_2 and $MoSe_2$ achieve the current density at η = 219 and 181 mV, respectively. These two values are comparable to or better than most previous results (see Table S1 in the Supporting Information).[13,16,17,20,40] Most importantly, the overpotential is further reduced on all alloyed nanoflakes. Improvements of 50−60 mV in comparison to MoS_2 and 10−20 mV in comparison to $MoSe_2$ are reproducibly measured, with the activity peaking at MoSSe (x = 0.5). Such tens of millivolts improvement is sufficiently significant in electrocatalysis.

Next, we analyzed the lower bound of the turnover frequency (TOF) at η = 150 mV. It was estimated on the basis of the electrochemically accessible surface areas of $MoS_{2(1-x)}Se_{2x}$ nanoflakes determined from their irreversible electrochemical oxidation in the anodic polarization (Figure S2 in the Supporting Information).[16] An interesting volcano-shaped trend is revealed as x is increased from 0 to 1 (Figure 4c). The best composition (i.e., MoSSe) has a TOF ∼2 times higher than that of MoS_2. In reality, only exposed edge sites of molybdenum dichalcogenides contribute to HER activity. We estimate that approximately 10% of atoms are situated at the edges on the basis of the nanoflake geometry. This translates to at least 1 order of magnitude underestimation of the actual TOF. Nevertheless, the comparison here does provide valuable insight into the relative intrinsic HER activity of $MoS_{2(1-x)}Se_{2x}$ alloys, given that they have largely similar morphologies (in other words, they may have similar fractions of edge atoms). In addition, impedance measurements were carried out at η = 150 mV (Figure S3 in the Supporting Information). The charge transfer resistances of $MoS_{2(1-x)}Se_{2x}$ nanoflakes vary in a trend in accordance with TOF estimations.

Furthermore, we performed Tafel analysis of the HER polarization curves, as shown in Figure 4d. The liner regions were fit by the Tafel equation with the slope information extracted and summarized in Table 1. MoS_2 exhibits a Tafel slope of 91 mV/decade, close to many literature values for 2H-MoS_2.[11,14,16,41] However, we do note that this number is substantially larger than that for MoS_2/rGO (∼40 mV/decade) reported by some of us previously.[15] The difference should not be taken as an indicator of the inferior quality of MoS_2 itself in

DOI: 10.1021/cs501970w
ACS Catal. 2015, 5, 2213−2219

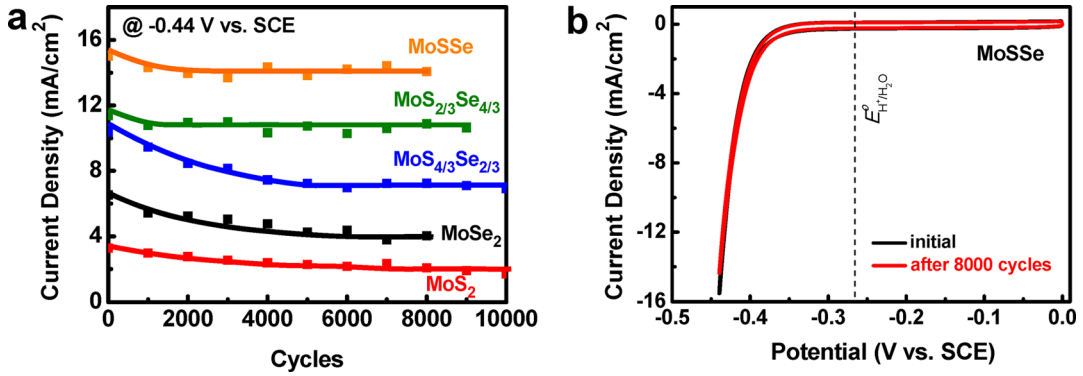

Figure 5. Cycling stability of $MoS_{2(1-x)}Se_{2x}$ nanoflake catalysts: (a) changes of HER cathodic current density (at −0.44 V vs SCE) with respect to the number of potential cycles; (b) CV curves of MoSSe before and after 8000 potential cycles. All of the nanoflake catalysts are highly durable.

this work (since it is similar to or better than values for most other MoS_2 electrocatalysts) but rather highlights the great benefit when graphene nanosheets were introduced as the conductive support for HER electrocatalysis. Such support effects are not the focus of our current study. Substitution of sulfur atoms with selenium leads to reduced Tafel slopes, probably afforded by the improved electrical conductivity with narrowing band gap. In particular, $MoS_{2(1-x)}Se_{2x}$ alloy nanoflakes having $0.5 \leq x \leq 1$ exhibit Tafel slopes in the range of 45−55 mV/decade, close to the theoretical value of 40 mV/decade when the Volmer−Heyrovsky reaction pathway is operative with electrochemical desorption of hydrogen as the rate-limiting step.[15,42] It is worth mentioning that even though the S-rich $MoS_{4/3}Se_{2/3}$ has an onset potential similar to that of the best alloy sample (MoSSe), its cathodic current density is quickly surpassed by Se-rich alloy catalysts at high overpotentials because of its inferior Tafel slope.

Finally, to demonstrate the long-term durability of these nanoflakes, we carried out continuous potential cycling up to 10000 cycles. Their polarization curves were periodically inspected every 1000 cycles, and the change of cathodic current density was plotted at −0.44 V vs SCE, as shown in Figure 5a. All five electrocatalysts show a gradual decrease in current density initially but stabilize after 1000−5000 cycles. The two best candidates are alloyed nanoflakes with $x = 1/2$ and 2/3, which exhibit current density retention of >93% and deliver 14.1 and 10.6 mA/cm^2, respectively, after >8000 cycles. Such activity loss translates to a negligible increment of overpotential in the polarization curve. Figure 5b compares polarization curves of MoSSe nanoflakes before and after the potential cycling. The latter curve almost retraces the initial shape even after 8000 cycles. This attests to the electrochemical durability of $MoS_{2(1-x)}Se_{2x}$ nanoflakes.

The above results unambiguously show that alloyed nanoflakes, especially with a nominal composition of MoSSe, have improved HER activity in comparison to either MoS_2 or $MoSe_2$. Their fully tunable chemical composition free of phase separation provides a new degree of freedom for continuously tailoring the electrocatalytic performance. Earlier theoretical calculations suggested that hydrogen adsorption is slightly too weak on sulfided Mo edges (ΔG_H = 80 meV) but slightly too strong on selenided Mo edges (ΔG_H = −140 meV).[8,22] By selecting the appropriate Se:S ratio, we may be able to adjust the hydrogen adsorption energy and achieve a ΔG_H value close to thermoneutral, consequently maximizing their HER activity. For catalysis on metals, theory predicts that the binding energy of an adsorbate to a metal surface is largely dependent on the d band electronic structure of the metal.[39] Even though the picture for oxide or sulfide catalysts is much more complex, it is believed that the d band electronic structure also greatly influences absorbate binding and thereby catalytic activity.[43,44] In this work, we have shown direct evidence of continuous modulation of molybdenum d band electronic structure by varying the Se:S ratio from the Mo 3d XPS spectrum (Figure 3c). A higher selenium content increases the d band filling of molybdenum and reduces its nominal oxidation state. As a result, we expect that the hydrogen adsorption energy on $MoS_{2(1-x)}Se_{2x}$ nanoflakes could be effectively tuned. The best HER activity observed with MoSSe may reflect its optimum hydrogen adsorption among the five compositions examined. Our conclusion is also supported by the recent observation that the HER activity of MoS_2 could be much improved when it was electrochemically reduced with lithium intercalation.[45]

4. CONCLUSIONS

In summary, through a high-temperature solution method, ultrathin $MoS_{2(1-x)}Se_{2x}$ alloy nanoflakes with monolayer or few-layer thicknesses were prepared. Their fully tunable chemical compositions free of phase separation allow progressive modulation of structures and properties. It is evidenced that the d band electronic structure of molybdenum is continuously modified upon the introduction of selenium. Our $MoS_{2(1-x)}Se_{2x}$ nanoflakes have high activity and durability for HER electrocatalysis with small overpotentials in the range of 80−100 mV and negligible activity loss up to 10000 potential cycles. Among them, alloyed nanoflakes—particularly MoSSe—exhibit improved performance in comparison to either MoS_2 or $MoSe_2$. We believe this results from their higher intrinsic activities with ΔG_H closer to thermoneutral. The current study explores the influence of chemical composition of molybdenum chalcogenides on their HER activity. It can be combined with other known effects (for example, the effect of a conductive carbon support) in the future design of non precious metal based HER electrocatalysts.

■ ASSOCIATED CONTENT

Supporting Information

The following file is available free of charge on the ACS Publications website at DOI: 10.1021/cs501970w.

A brief survey of MoS_2 and $MoSe_2$ HER electrocatalysts reported in the literature, polarization curves before Ar annealing, CV curves in the anodic potential region

DOI: 10.1021/cs501970w
ACS Catal. 2015, 5, 2213−2219

showing their irreversible electrochemical oxidation, and impedance measurements (PDF)

AUTHOR INFORMATION

Corresponding Authors

*E-mail for Z.L.: zliu@suda.edu.cn.
*E-mail for Y.L.: yanguang@suda.edu.cn.

Author Contributions

§Q.G. and L.C. contributed equally to this paper

Notes

The authors declare no competing financial interest.

ACKNOWLEDGMENTS

We acknowledge support from the National Natural Science Foundation of China (51302180, 51222203, 51002100, 51132006, 51472173), the National "973" Program of China (2011CB911002, 2012CB932601), the National Natural Science Foundation of Jiangsu Province (BK20130005, BK20130305, BK20140302), the postdoctoral research program of Jiangsu Province (1202044C), the postdoctoral science foundation of China (2013M531400), Jiangsu Key Laboratory for Carbon-Based Functional Materials and Devices, and Collaborative Innovation Center of Suzhou Nano Science and Technology.

REFERENCES

(1) Bard, A. J.; Fox, M. A. *Acc. Chem. Res.* **1995**, *28*, 141.
(2) Morales-Guio, C. G.; Stern, L.-A.; Hu, X. *Chem. Soc. Rev.* **2014**, *43*, 6555.
(3) Walter, M. G.; Warren, E. L.; McKone, J. R.; Boettcher, S. W.; Mi, Q. X.; Santori, E. A.; Lewis, N. S. *Chem. Rev.* **2010**, *110*, 6446.
(4) Li, Y. *IEEE Nanotechnol. Mag.* **2014**, *8*, 22.
(5) Trasatti, S. *J. Electroanal. Chem. Interfacial Electrochem.* **1972**, *39*, 163.
(6) Chhowalla, M.; Shin, H. S.; Eda, G.; Li, L.-J.; Loh, K. P.; Zhang, H. *Nat. Chem.* **2013**, *5*, 263.
(7) Yang, J.; Shin, H. S. *J. Mater. Chem. A* **2014**, *2*, 5979.
(8) Hinnemann, B.; Moses, P. G.; Bonde, J.; Jørgensen, K. P.; Nielsen, J. H.; Horch, S.; Chorkendorff, I.; Nørskov, J. K. *J. Am. Chem. Soc.* **2005**, *127*, 5308.
(9) Jaramillo, T. F.; Jorgensen, K. P.; Bonde, J.; Nielsen, J. H.; Horch, S.; Chorkendorff, I. *Science* **2007**, *317*, 100.
(10) Lukowski, M. A.; Daniel, A. S.; Meng, F.; Forticaux, A.; Li, L.; Jin, S. *J. Am. Chem. Soc.* **2013**, *135*, 10274.
(11) Voiry, D.; Salehi, M.; Silva, R.; Fujita, T.; Chen, M.; Asefa, T.; Shenoy, V. B.; Eda, G.; Chhowalla, M. *Nano Lett.* **2013**, *13*, 6222.
(12) Xie, J.; Zhang, H.; Li, S.; Wang, R.; Sun, X.; Zhou, M.; Zhou, J.; Lou, X. W. D.; Xie, Y. *Adv. Mater.* **2013**, *25*, 5807.
(13) Kibsgaard, J.; Chen, Z. B.; Reinecke, B. N.; Jaramillo, T. F. *Nat. Mater.* **2012**, *11*, 963.
(14) Kong, D. S.; Wang, H. T.; Cha, J. J.; Pasta, M.; Koski, K. J.; Yao, J.; Cui, Y. *Nano Lett.* **2013**, *13*, 1341.
(15) Li, Y. G.; Wang, H. L.; Xie, L. M.; Liang, Y. Y.; Hong, G. S.; Dai, H. J. *J. Am. Chem. Soc.* **2011**, *133*, 7296.
(16) Bonde, J.; Moses, P. G.; Jaramillo, T. F.; Nørskov, J. K.; Chorkendorff, I. *Faraday Discuss.* **2009**, *140*, 219.
(17) Wang, H. T.; Kong, D. S.; Johanes, P.; Cha, J. J.; Zheng, G. Y.; Yan, K.; Liu, N. A.; Cui, Y. *Nano Lett.* **2013**, *13*, 3426.
(18) Mao, S.; Wen, Z.; Ci, S.; Guo, X.; Ostrikov, K. K.; Chen, J. *Small* **2014**, *11*, 508.
(19) Zhang, Y.; Gong, Q.; Li, L.; Yang, H.; Li, Y.; Wang, Q. *Nano Res.* **2014**, DOI: 10.1007/s12274-014-0590-0.
(20) Kong, D.; Wang, H.; Cha, J. J.; Pasta, M.; Koski, K. J.; Yao, J.; Cui, Y. *Nano Lett.* **2013**, *13*, 1341.
(21) Saadi, F. H.; Carim, A. I.; Velazquez, J. M.; Baricuatro, J. H.; McCrory, C. C.; Soriaga, M. P.; Lewis, N. S. *ACS Catal.* **2014**, *4*, 2866.
(22) Tang, H.; Dou, K.; Kaun, C.-C.; Kuang, Q.; Yang, S. *J. Mater. Chem. A* **2014**, *2*, 360.
(23) Gong, Y. J.; Liu, Z.; Lupini, A. R.; Shi, G.; Lin, J. H.; Najmaei, S.; Lin, Z.; Elias, A. L.; Berkdemir, A.; You, G.; Terrones, H.; Terrones, M.; Vajtai, R.; Pantelides, S. T.; Pennycook, S. J.; Lou, J.; Zhou, W.; Ajayan, P. M. *Nano Lett.* **2014**, *14*, 442.
(24) Feng, Q. L.; Zhu, Y. M.; Hong, J. H.; Zhang, M.; Duan, W. J.; Mao, N. N.; Wu, J. X.; Xu, H.; Dong, F. L.; Lin, F.; Jin, C. H.; Wang, C. M.; Zhang, J.; Xie, L. M. *Adv. Mater.* **2014**, *26*, 2648.
(25) Mann, J.; Ma, Q.; Odenthal, P. M.; Isarraraz, M.; Le, D.; Preciado, E.; Barroso, D.; Yamaguchi, K.; Palacio, G. V.; Nguyen, A.; Tran, T.; Wurch, M.; Nguyen, A.; Klee, V.; Bobek, S.; Sun, D. Z.; Heinz, T. F.; Rahman, T. S.; Kawakami, R.; Bartels, L. *Adv. Mater.* **2014**, *26*, 1399.
(26) Li, H.; Duan, X.; Wu, X.; Zhuang, X.; Zhou, H.; Zhang, Q.; Zhu, X.; Hu, W.; Ren, P.; Guo, P.; Ma, L.; Fan, X.; Wang, X.; Xu, J.; Pan, A.; Duan, X. *J. Am. Chem. Soc.* **2014**, *136*, 3756.
(27) Cheng, L.; Huang, W. J.; Gong, Q. F.; Liu, C. H.; Liu, Z.; Li, Y. G.; Dai, H. J. *Angew. Chem., Int. Ed.* **2014**, *53*, 7860.
(28) Du, Y.; Yin, Z.; Zhu, J.; Huang, X.; Wu, X.-J.; Zeng, Z.; Yan, Q.; Zhang, H. *Nat. Commun.* **2012**, *3*, 1177.
(29) Thomson, J. W.; Nagashima, K.; Macdonald, P. M.; Ozin, G. A. *J. Am. Chem. Soc.* **2011**, *133*, 5036.
(30) Walker, B.; Agrawal, R. *Chem. Commun.* **2014**, *50*, 8331.
(31) Yu, W. W.; Peng, X. *Angew. Chem., Int. Ed.* **2002**, *41*, 2368.
(32) Vrubel, H.; Merki, D.; Hu, X. *Energy Environ. Sci.* **2012**, *5*, 6136.
(33) Remskar, M.; Mrzel, A.; Skraba, Z.; Jesih, A.; Ceh, M.; Demšar, J.; Stadelmann, P.; Lévy, F.; Mihailovic, D. *Science* **2001**, *292*, 479.
(34) Nath, M.; Govindaraj, A.; Rao, C. *Adv. Mater.* **2001**, *13*, 283.
(35) Tenne, R.; Redlich, M. *Chem. Soc. Rev.* **2010**, *39*, 1423.
(36) Margulis, L.; Salitra, G.; Tenne, R.; Talianker, M. *Nature* **1993**, *365*, 113.
(37) Li, H.; Zhang, Q.; Yap, C. C. R.; Tay, B. K.; Edwin, T. H. T.; Olivier, A.; Baillargeat, D. *Adv. Funct. Mater.* **2012**, *22*, 1385.
(38) Shaw, J. C.; Zhou, H. L.; Chen, Y.; Weiss, N. O.; Liu, Y.; Huang, Y.; Duan, X. F. *Nano Res.* **2014**, *7*, 511.
(39) Hammer, B.; Nørskov, J. K. *Adv. Catal.* **2000**, *45*, 71.
(40) Jia, L.; Sun, X.; Jiang, Y.; Yu, S.; Wang, C. *Adv. Funct. Mater.* **2014**, DOI: 10.1002/adfm.201401814.
(41) Gopalakrishnan, D.; Damien, D.; Shaijumon, M. M. *ACS Nano* **2014**, *8*, 5297.
(42) Conway, B.; Tilak, B. *Electrochim. Acta* **2002**, *47*, 3571.
(43) Tsai, C.; Chan, K.; Norskov, J. K.; Abild-Pedersen, F. *J. Phys. Chem. Lett.* **2014**, *5*, 3884.
(44) Akhade, S. A.; Kitchin, J. R. *J. Chem. Phys.* **2012**, *137*, 084703.
(45) Wang, H.; Lu, Z.; Xu, S.; Kong, D.; Cha, J. J.; Zheng, G.; Hsu, P.-C.; Yan, K.; Bradshaw, D.; Prinz, F. B.; Cui, Y. *Proc. Natl. Acad. Sci. U. S. A.* **2013**, *110*, 19701.

DOI: 10.1021/cs501970w
ACS Catal. 2015, 5, 2213−2219